Journal of Magnetism and Magnetic Materials 502 (2020) 166595

Contents lists available at ScienceDirect

Journal of Magnetism and Magnetic Materials

journal homepage: www.elsevier.com/locate/jmmm

Research articles

Structural, electronic, vibrational and magnetic properties of Zn^{2+} substituted $MnCr_2O_4$ nanoparticles

K. Manjunatha[a], V. Jagadeesha Angadi[b,*], Renan A.P. Ribeiro[c], Elson Longo[c], Marisa C. Oliveira[d], Mauricio R.D. Bomio[d], Sergio R. de Lázaro[e], Shidaling Matteppanavar[f], S. Rayaprol[g], P.D. Babu[g], Mahaboob Pasha[a]

[a] Department of Physics, School of Engineering, Presidency University, Bangalore 560064, India
[b] Deparment of Physics, P.C. Jabin Science College, Hubballi 580031, India
[c] CDMF-UFSCar, Universidade Federal de São Carlos, PO Box 676, 13565–905 São Carlos, SP, Brazil
[d] LSQM- Laboratório de Síntese Química de Materiais, DEMat, Universidade Federal do Rio Grande do Norte - UFRN, P.O. Box 1524, 59078-970 Natal, RN, Brazil
[e] Department of Chemistry, Av. Gen. Carlos Cavalcanti, no 4748, Zip-Code: 84030-000, Ponta Grossa, Paraná, Brazil
[f] Department of Physics, Basavaprabhu Kore Arts, Science and Commerce College, 591201 Chikodi, India
[g] UGC-DAE CSR, Mumbai Centre, BARC Campus, Trombay, Mumbai 400085, India

ARTICLE INFO

Keywords:
Neutron diffraction
Solution combustion method
Raman spectra
Antiferromagnetic
DFT calculations

ABSTRACT

In the present investigation, we report the structural, vibrational, electronic and magnetic properties of $Mn_{0.5}Zn_{0.5}Cr_2O_4$ nanoparticles fabricated by the solution combustion method and complemented by Density Functional theory (DFT) calculations. X-ray diffraction (XRD), Neutron diffraction, X-ray photoelectron spectroscopy and Raman analysis confirms the formation of single-phase with spinel cubic structure. The average crystallite size was found to be 8 nm. The theoretical calculations suggest that Zn-doping on the $MnCr_2O_4$ matrix induces a unit cell contraction associated with structural distortions along both [AO_4] (A = Mn, Zn) and [CrO_6] clusters, in agreement with the experimental evidence. These structural distortions contribute to narrowing the band-gap of $Mn_{0.5}Zn_{0.5}Cr_2O_4$ from disturbed energy levels in the vicinity of Fermi level. Field dependent magnetization confirms that the samples exhibit paramagnetic nature at 300 K and antiferromagnetic nature at 3 K. In the theoretical context, the exchange coupling constant for pure and Zn^{2+} substituted $MnCr_2O_4$ materials were calculated confirming the dominant antiferromagnetic character of Cr-Cr interactions. The temperature dependent susceptibility reveals that the magnetic transition from paramagnetic phase to antiferromagnetic phase occurs at 19 K (T_N). The spin frustration factor of $Mn_{0.5}Zn_{0.5}Cr_2O_4$ is found to be 22 K. Hence, our experimental and theoretical result suggests that synthesized materials are useful for low and high frequency applications.

1. Introduction

Spinel chromite nanoparticles have recently attracted remarkable interest due to their superior magnetic properties, showing great potential for technological applications as a solar absorber, gas sensors, dye substrate for film growth, drug delivery system, power transformers, data storage media, telecommunication systems, random access memories and radar absorbing points [1–5].

In ACr_2O_4 nanoparticles having spinel structure, the A^{2+} ions occupy the tetrahedral site while Cr^{3+} ions are in the center of six-fold octahedral site. The magnetic interaction for this class of materials along the A- and Cr-lattices can induce intriguing magnetic properties [6,7]. In chromite spinels with magnetic A-site cations, such as $NiCr_2O_4$, $FeCr_2O_4$ and $CoCr_2O_4$ spinels, collinear ferrimagnetic phase at Curie temperatures (T_c) can be found in the range of 70–100 K. In addition, $FeCr_2O_4$ and $CoCr_2O_4$ exhibit both spiral magnetic and ferrimagnetic ordering [7–9]. Furthermore, $MnCr_2O_4$ is a representative member of spinel chromites which displays a long-range ferrimagnetic spin order (T_c = 41–52 K) accompanied by transition into a short-range spiral spin order at T_S = 14–20 K [10].

On the other hand, chromite spinels with non-magnetic A-site atoms such as $MgCr_2O_4$, $ZnCr_2O_4$ and $CdCr_2O_4$ are geometrically-frustrated antiferromagnets below Neel's temperature (T_N) of 12.7 K, 12.5 K, 8 K, respectively [5]. In this case, the frustration occurs from the unsatisfied

* Corresponding author.
E-mail address: jagadeeshbub@gmail.com (V. Jagadeesha Angadi).

https://doi.org/10.1016/j.jmmm.2020.166595
Received 31 October 2019; Received in revised form 7 February 2020; Accepted 8 February 2020
Available online 11 February 2020

antiferromagnetic spin arrangement along the Cr sublattice. However, some nanoparticles can present paramagnetic behavior, as reported by Mousavi *et al.* who synthesized $ZnCr_2O_4$ nanoparticles with paramagnetic behavior, although bulk $ZnCr_2O_4$ is antiferromagnetic, which was attributed to the finite size effects [11].

Therefore, the A-site cations play a fundamental role for tuning the main properties of spinel chromites [12–16]. Mixed composition containing both magnetic and non-magnetic A-site cations showed interesting magnetic, electronic and optical properties. In particular, Zn-modified $MnCr_2O_4$ spinels has attracted remarkable interest due to the intriguing magnetic properties [14–16]. However, understanding magnetic evolution and its molecular structure fingerprints remains unclear.

Innumerous synthesis methods are available for preparing spinel chromite materials such as the sol–gel method, solid state reaction, sonochemical, coprecipitation, citrate gel combustion, solution combustion and the precursor thermolysis method [3,4]. Among all the methods, the solution combustion method is very effective and suitable to prepare spinel chromate nanoparticles with good control of stoichiometry and purity. The solution combustion method was introduced by Patil [17]. This method is very easy, less time consuming, energy efficient, and requires very low temperature to form single phase materials. In the solution combustion method, the physicochemical properties of a product such as particle size, crystallinity, composition, purity, surface area, morphology, degree and nature of the aggregate can be influenced by fuel type [13,17].

In this context, the present work aims to report the structural, electronic, vibrational, and magnetic properties of Zn^{2+} substituted $MnCr_2O_4$ nanoparticles obtained by the solution combustion method using a mixture of urea and glucose as fuels. Theoretical calculations were conducted to determine the magnetic interactions for this material for the first time, confirming the dominant role of Cr sublattice interaction. A detailed discussion about the magnetic evolution based on the disorder effect induced by the substitution of Mn^{2+} ions by non-magnetic Zn^{2+} ones in $Mn_{0.5}Zn_{0.5}Cr_2O_4$ nanoparticles is also presented, unveiling the intriguing magnetic properties.

2. Experimental details

2.1. Metal nitrates (oxidizers) and reducing agents (fuels)

For the synthesis of $Mn_{0.5}Zn_{0.5}Cr_2O_4$ nanoparticles we used manganese nitrate [$Mn(NO_3)_2{\cdot}4H_2O$] (Sigma-Aldrich, Purity 99.0%), molecular weight 251.01 g/mol; zinc nitrate [$Zn(NO_3)_2{\cdot}6H_2O$] (Sigma-Aldrich, Purity ≥ 98.0%), molecular weight 297.48 g/mol; Chromium nitrate [$Cr(NO_3)_2{\cdot}9H_2O$] (LOBA CHEMI, Purity 97.0%), molecular weight 485.07 g/mol; and reducing agents were glucose [$C_6H_{12}O_6$] (Glucomin – D, Purity 99.4%), molecular weight 180.156 g/mol; and urea [NH_2CONH_2] (Fisher Scientific, Purity 99.0%), molecular weight 60.06 g/mol.

2.2. Solution combustion method

Zn^{2+}substituted $MnCr_2O_4$ nanoparticles were prepared by the solution combustion method using metal nitrates and a mixture of (reducing agents) NH_2CONH_2 (urea) and $C_6H_{12}O_6$ (glucose) as fuels. The ratio of oxidizers and fuels in the solution combustion method is maintained to unity [18]. The stoichiometry amount of all metal nitrates and fuels are weighed and added into the beaker one by one. All these weighed metal nitrates and fuels are diluted with distilled water and then mixed by using a magnetic stirrer for about 45 min at a speed of 1200 revolution per minute to obtain a homogeneous solution. This homogeneous solution was kept inside a preheated muffle furnace at 450 °C. This solution is first heated, boiled, frothed and subsequently ignited. This process will be completed within 20 min, obtaining powder nanoparticles. The obtained powder nanoparticles are then put into an agate mortar and pestle to obtain fine powder. Fig. 1 shows the flow chart of the solution combustion method for synthesis of Zn^{2+} substituted $MnCr_2O_4$ nanoparticles.

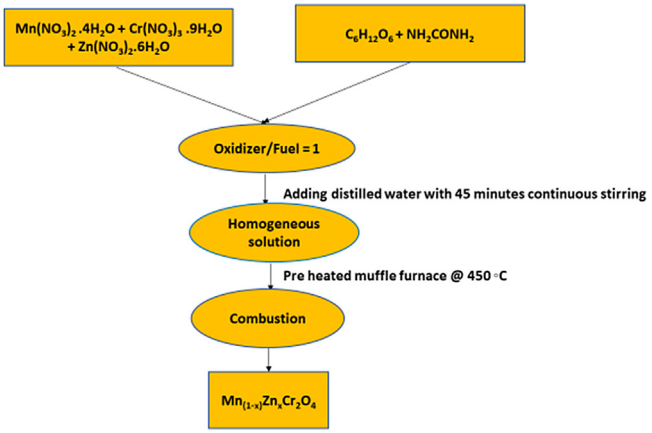

Fig. 1. Flow chart of the solution combustion method for synthesis of Zn^{2+} substituted $MnCr_2O_4$ nanoparticles.

2.3. Characterizations

The synthesized sample was characterized by X-Ray Diffractometric technique (XRD) and the diffractogram was obtained at 2θ in the range from 10° to 80° under a step size of 0.02°, which is done by using Cu-K_α radiation of wavelength (λ) of 1.5404 Å. The XRD data was fitted by using full proof software to understand the crystalline nature and structure. The Neutron Powder Diffraction (NPD) measurement was carried out with finely grained powder of the Zn^{2+} substituted $MnCr_2O_4$ sample packed in a vanadium container at room temperature, which was done by using a focusing crystal-based powder diffractometer at a wavelength of 1.48 Å at room temperature, at the UGC-DAE Consortium for Scientific Research beam line (PD-3) at the Dhruva reactor in Trombay, India. The NPD diffractogram was obtained at 2θ in the range of 6–119° at the step size of 0.037°.

The elemental composition of the Zn^{2+} substituted $MnCr_2O_4$ was analyzed through X-ray photoelectron spectroscopy (XPS) analysis conducted in a Vacuum Generator (VG) ESCALABMKII spectrometer upgraded AlK_α source fitted with a XR4 twin anode. This source was operated at 1486.6 eV energy with 300 W power. Raman spectrum was obtained by using Laser confocal Raman spectrometer in the wavenumber range from 100 to 800 cm^{-1} to study the vibrational modes. The field dependent and temperature dependent susceptibility were performed using a 7 Tesla SQUID magnetometer from Quantum Design with a temperature range going down to 1.8 K and magnetic field measured up to ± 90 kOe.

2.4. Computational details

Quantum-mechanical calculations in the framework of the Density Functional Theory (DFT) were carried out using the B3LYP exchange correlation functional implemented in CRYSTAL17 code [19–21] in order to obtain theoretical insight into the structural, magnetic and electronic properties of Zn^{2+} substituted $MnCr_2O_4$ oxide. Thus, pure $MnCr_2O_4$ was modelled in a normal spinel configuration considering the primitive unit cell of cubic symmetry (*Fd-3m*) containing two $MnCr_2O_4$ units (14-atoms). Aiming to represent the crystalline structure of the 50 mol % Zn^{2+} substituted $MnCr_2O_4$, $Mn_{0.5}Zn_{0.5}Cr_2O_4$, a conventional cubic unit cell containing four $MnCr_2O_4$ units (56-atoms) was used, where half of the Mn^{2+} sites were substituted by Zn^{2+} cations, as depicted in Fig. 2. Both atomic positions and unit cell parameters were relaxed in both cases as a function of the system's total energy. The convergence criteria for mono and bielectronic integrals were both

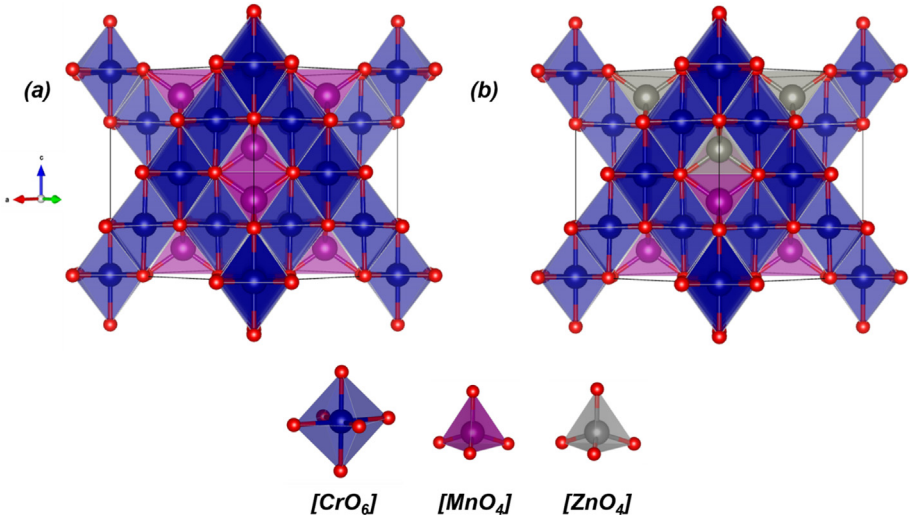

Fig. 2. Conventional unit cell for (a) $MnCr_2O_4$ and (b) $Mn_{0.5}Zn_{0.5}Cr_2O_4$ materials. The purple, gray, blue and red balls correspond to Mn, Zn, Cr and O atoms, respectively. The gray, purple and blue polyhedral correspond to $[ZnO_4]$, $[MnO_4]$ and $[CrO_6]$ clusters, respectively.

were set to 10^{-8} Hartree, while the RMS gradient, RMS displacement, maximum gradient and maximum displacement were set to 3×10^{-4}, 1.2×10^{-3}, 4.5×10^{-4} and 1.8×10^{-3} a.u., respectively. Regarding the density matrix diagonalization, the reciprocal space net was described by a dense mesh consisting of a shrinking factor set to $8 \times 8 \times 8$, corresponding to 29 k-points in accordance with the Monkhorst-Pack method [22]. The accuracy in evaluating the Coulomb and exchange series was controlled by five thresholds for which the adopted values are 10^{-8}, 10^{-8}, 10^{-8}, 10^{-8} and 10^{-16}. Zn, Mn, Cr were described by all-electron 86-411d41G basis set in all calculations, and the O atoms were described by 8-411G* [23–25].

The magnetic properties of pure and Zn^{2+} substituted $MnCr_2O_4$ materials were investigated considering a set of four collinear models described as: (i) ferromagnetic model (FEM), where the spins for all neighbors are parallel ordered; (ii) ferrimagnetic-1 model (FIM-1), for which the spins of Cr-site are parallel to each other, but antiparallel ordered to Mn; (iii) ferrimagnetic-2 model (FIM-2), where each spin of Mn are antiparallel to each other, while Cr-site spins are ferromagnetic; and (iv) ferrimagnetic-3 model (FIM-3), where each spin of Cr nearest neighbors are antiparallel ordered to each other, while Mn-site spins are ferromagnetic. The exchange coupling constant was computed from the energy difference between the magnetic configurations using the Ising model, which enables calculating the coupling constants J from the energy difference of the magnetic states, since the unpaired electrons are well-defined. The exchange coupling constants herein are described by the equations: [26–28]

$$\widehat{H}_{ising} = \sum J_{ij} \widehat{S}_{iz} \widehat{S}_{jz} \quad (1)$$

$$\Delta E_{FIM-FEM} = -2 \sum Z_{ij} S_i S_j J_{ij} \quad (2)$$

Eqs. (1) and (2) involve the number of the atom neighbors i-j (Z), the electronic spin of different species (S) and coupling constant between the species (J). The summation usually extends to first or second atom neighbors i-j, where i and j correspond to different magnetic sites, without double counting. This proposal can be applied to the four models previously proposed, and the coupling constants ($J_{Mn\text{-}Mn}$, $J_{Cr\text{-}Mn}$, $J_{Cr\text{-}Cr}$) for pure $MnCr_2O_4$ can be calculated from the equations:

$$\Delta E_{FIM1-FEM} = 48\, J_{Cr-Mn} S_{Cr} S_{Mn} \quad (3)$$

$$\Delta E_{FIM2-FEM} = 12 J_{Cr-Mn} S_{Cr} S_{Mn} + 8 J_{Mn-Mn} S_{Mn}^2 \quad (4)$$

$$\Delta E_{FIM3-FEM} = 12 J_{Cr-Mn} S_{Cr} S_{Mn} + 12 J_{Cr-Cr} S_{Cr}^2 \quad (5)$$

Similar equations can be used for $Mn_{0.5}Zn_{0.5}Cr_2O_4$ material, considering the existence of $J_{Cr\text{-}Mn}$ and $J_{Cr\text{-}Cr}$ exchange coupling constants. In this case, $J_{Mn\text{-}Mn}$ are not considered because of the larger Mn-Mn distance in Zn substituted material, making the $J_{Mn\text{-}Mn}$ coupling constant a third-neighbor interaction. Therefore, the proposed equations in this case were:

$$\Delta E_{FIM1-FEM} = 96\, J_{Cr-Mn} S_{Cr} S_{Mn} \quad (6)$$

$$\Delta E_{FIM3-FEM} = 24 J_{Cr-Mn} S_{Cr} S_{Mn} + 24 J_{Cr-Cr} S_{Cr}^2 \quad (7)$$

3. Results and discussion

3.1. Effect of synthesis process on the structure of $Mn_{0.5}Zn_{0.5}Cr_2O_4$ nanoparticles

The Rietveld refined XRD patterns of $Mn_{0.5}Zn_{0.5}Cr_2O_4$ nanoparticles synthesized via the solution combustion route are shown in Fig. 3. Peak positions in the XRD data confirm the single phase having spinel cubic structure with *Fd-3m* space group. The non-existence of additional peaks in the XRD patterns clearly confirms that there is no impurity peak. The observed XRD pattern peaks match with the JCPDS [33–892] [29]. The lattice parameter of the $Mn_{0.5}Zn_{0.5}Cr_2O_4$ was found to be 8.358 Å, which is less than the reported lattice parameter of $MnCr_2O_4$

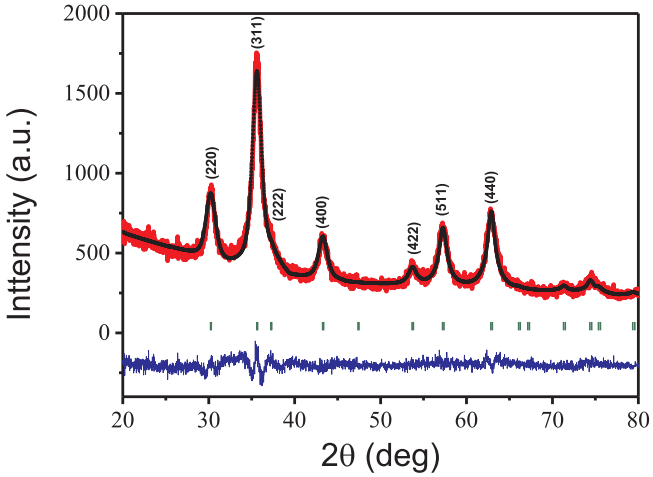

Fig. 3. X-ray diffraction patterns of the as-synthesized $Mn_{0.5}Zn_{0.5}Cr_2O_4$ nanoparticles.

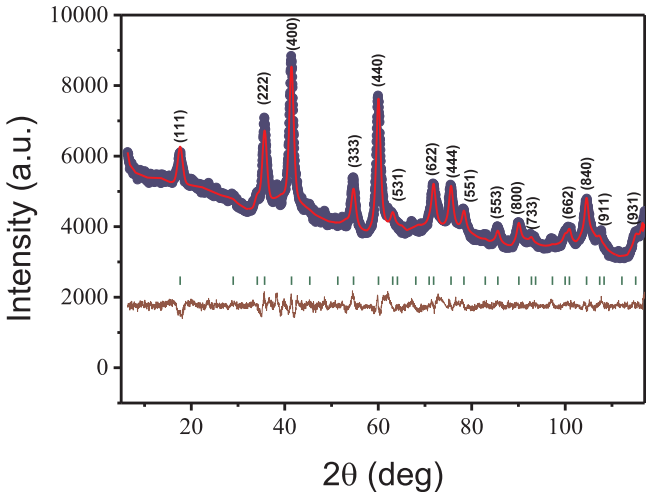

Fig. 4. Neutron diffraction pattern of the as synthesized of $Mn_{0.5}Zn_{0.5}Cr_2O_4$nanoparticles.

nanoparticles [30]. The lattice parameter decreases after substituting the 50 mol % Zn^{2+} due to the difference in ionic radius between Mn^{2+}(0.66 Å) and Zn^{2+} (0.6 Å) ions at the tetrahedral site. The crystallite size and strain was calculated by using the Scherer method, being $d = k\lambda/\beta cos\theta$ and $\varepsilon = \beta cos\theta/4$ respectively, where k is the Scherer constant, λ is the wavelength of CuK_α line radiation, β is the full width half maximum and θ is the diffraction angle. The average crystallite size and lattice strain were found to be 8 nm and 4.41 × 10^{-3}% respectively. The magnetic hopping length L_A and L_B was calculated using these equations $L_A = \frac{a\sqrt{3}}{4}$, $L_B = \frac{a\sqrt{2}}{4}$respectively, where a is the lattice parameter [31]. Hopping length is helpful to identify the distance between the magnetic ions in the tetrahedral and octahedral sites. The hopping lengths were found to be L_A = 3.618 Å and L_B = 2.954 Å. The volume of the $Mn_{0.5}Zn_{0.5}Cr_2O_4$ nanoparticles was found to be 583.85 $Å^3$.

3.2. Neutron diffraction analysis

NPD patterns were measured at room temperature in order to study the crystallinity structure along with the paramagnetic structure. Fig. 4 shows the Rietveld refinement neutron diffraction patterns of $Mn_{0.5}Zn_{0.5}Cr_2O_4$ nanoparticles. The R factors for cubic structure were obtained from the Rietveld refined neutron diffraction analysis as Bragg R-factor = 2.405, R_F-factor = 1.742, R_P-factor = 22.0, R_{WP}-factor = 16.9, R_{EXP}-factor = 12.55, and goodness of fit χ^2 = 1.81. These R-factors are good enough to show the fit precision. It can clearly be seen from the neutron diffraction pattern that all peaks match well with the spinel cubic structure [32]. The structure is characterized by the AB_2O_4 spinel structure, where A is the tetrahedral site and B is the octahedral site. Tetrahedral sites here are occupied by Mn^{2+} and substitute Zn^{2+}, whereas the octahedral sites are occupied by Cr^{3+} ions, indicating that there is no mixing of Zn^{2+} ions at the A-sites and B-sites. The Wyckoff position for the Mn^{2+}/Zn^{2+} atoms is 8a, while for Cr^{3+} atoms it is 16d, and for O^{2-} ions it is 32e sites in the framework of the *Fd-3m* space group. The lattice parameter of the $Mn_{0.5}Zn_{0.5}Cr_2O_4$ nanoparticles at room temperature is found to be 8.366 Å. This lattice parameter value matches well with the lattice parameter obtained from XRD data.

3.3. XPS analysis

The obtained XPS spectra for $Mn_{0.5}Zn_{0.5}Cr_2O_4$ nanoparticles and each element (such as Mn2P, Zn2P, Cr2P and O1S) is presented in Fig. 5(a–e). In all XPS spectra, a red line indicates the raw XPS spectrum data and a green line indicates the fitted XPS spectrum data. Fig. 5(a) shows the complete survey spectrum of $Mn_{0.5}Zn_{0.5}Cr_2O_4$ nanoparticles, as well as the presence of each element.

The core spectra of Mn2P is shown in Fig. 5(b). The core spectra of Mn2P indicates the peak at 653.5 eV and 641.55 eV, respectively corresponding to the $Mn2P_{1/2}$ and $Mn2P_{3/2}$ [33]. Both peaks at binding energies of 653.5 eV and 641.55 eV for Mn^{2+} were only observed in the seed nanoparticles. The Mn2P core spectrum of $Mn_{0.5}Zn_{0.5}Cr_2O_4$ nanoparticles does not show any additional peak.

The core spectra of Zn2P is shown in Fig. 5(c). The core spectra of Zn2P reveal the $Zn2P_{3/2}$ binding energy centered at 1021.35 eV and the $Zn2P_{1/2}$ binding energy centered at 1044.4 eV, which are the characteristic values of the oxidation state of Zn^{2+} in $Mn_{0.5}Zn_{0.5}Cr_2O_4$ nanoparticles. These results indicate the presence of Zn^{2+} in the surface morphologies of $Mn_{0.5}Zn_{0.5}Cr_2O_4$. The binding energy difference between $Zn2P_{1/2}$ and $Zn2P_{3/2}$ is 23.05 eV for $Mn_{0.5}Zn_{0.5}Cr_2O_4$ nanoparticles.

Fig. 5(d) shows the core spectrum of Cr2P, which indicates the presence of two strong peaks related with $Cr2P_{1/2}$ and $Cr2P_{3/2}$ binding energies centered at 586.3 eV and 576.3 eV, respectively. The peak at 576.3 eV confirms that Cr^{3+} ions are located at octahedral sites and exposed on the surface of the spinel samples, being considered as active sites. The peak at 586.3 eV indicates the presence of Cr^{6+} ions in spinel samples as reported by Sloczynski et al. [34], being attributed to the presence of small percentages of Cr^{6+} in the sample or surface oxidation.

The core spectrum of O1S is shown in Fig. 5(e). The oxygen core spectra of the asymmetric peak at 530.35 eV was attributed to the lattice oxygen and one weak peak at 531.3 eV was attributed to superficial adsorbed oxygen (hydroxyl oxygen), which are characteristic of the oxidation of O^{2-} in $Mn_{0.5}Zn_{0.5}Cr_2O_4$ nanoparticles. These adsorbed oxygen peaks can be attributed to a variety of species such as oxygen ions in a low coordination condition, surface chemisorbed oxygen, hydroxyl and an amount of oxygen containing surface contamination [35].

3.4. Raman analysis

The Raman spectra of $Mn_{0.5}Zn_{0.5}Cr_2O_4$ nanoparticles in the range of 100–800 cm^{-1} is depicted in Fig. 6. This spectrum clearly shows the existence of four bands at 172, 486, 547 and 661 cm^{-1}. According to group theory, $Mn_{0.5}Zn_{0.5}Cr_2O_4$ is a normal spinel spectra and has five phonon modes (A_{1g} + E_g + $3F_{2g}$). The phonon modes can be observed at approximately 172 cm^{-1}(F_{2g}(3)), 486 cm^{-1} (F_{2g}(2)), 547 cm^{-1} (F_{2g}(1)) and 661 cm^{-1} (A_{1g}). The lower frequency phonon vibrations F_{2g}(3) greatly depend on the octahedral site of Cr^{3+} ions and was observed at 172 cm^{-1}. The higher frequency phonon vibrations F_{2g}(2) greatly depends on the tetrahedral site of Mn^{2+} and Zn^{2+} ions, and was observed at 486 cm^{-1}. The peak at 547 cm^{-1} was attributed to the stretching modes of Cr-O-Cr. In comparison with the Raman spectra of $ZnCr_2O_4$ by Wang et al. [36], the broad Raman band at 661 cm^{-1} is attributed to the partial position disorder of the cations in the spinel structure, i.e. the so-called antisite defect [37].

3.5. Field dependent magnetization

Fig. 7 shows the field dependent magnetization (M−H loop) of $Mn_{0.5}Zn_{0.5}Cr_2O_4$ nanoparticles at 3 K and 300 K (Room temperature). The maximum magnetic field applied was 8.4 T. The black line shows the M−H curve at 300 K, which clearly indicates the paramagnetic behavior of the sample; we cannot observe any hysteresis loss at 300 K in this loop, as the magnetization shows the linear nature with an applied magnetic field up to 8.4 T. However, the sample exhibits hysteresis loss in the M−H loop at 3 K. The M−H loop reveals an antiferromagnetic nature of the sample with remanent magnetization of (M_r) 0.377 emu/g and saturation magnetization (M_s) of 3.667 emu/g

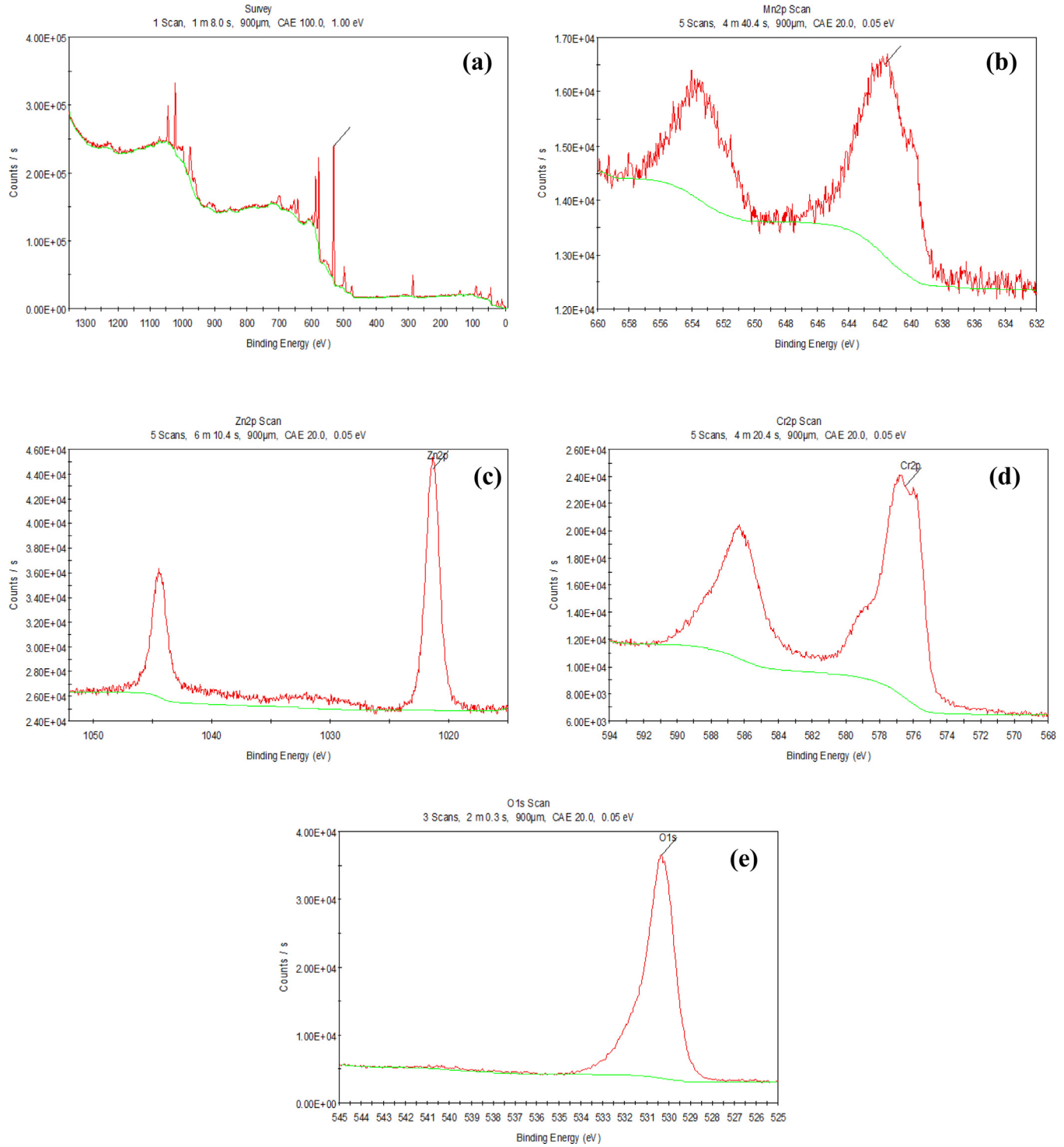

Fig. 5. XPS of the as-synthesized of $Mn_{0.5}Zn_{0.5}Cr_2O_4$nanoparticles for (a) wide range spectra, (b) Mn2P core spectra, (c) Zn2P core spectra, (d) Cr2P core spectra and (e) O1S core spectra.

[38]. The coercivity field was estimated as 1578.35 Oe by using the mean of negative coercivity ($-H_c$) and positive coercivity ($+H_c$) along the M−H loop of the field axis. The reduced remanence (S) was calculated by using this equation: $S = M_r/M_s$, which was found to be 0.102. The uniaxial anisotropy (K_u) was calculated by using this equation; $K_u = \frac{H_c X M_s}{0.985}$ and uniaxial anisotropy was found to be 5875.94 erg/Oe. The cubic anisotropy (K_c) was calculated by using this equation: $K_c = \frac{H_c X M_s}{0.64}$ and cubic anisotropy was found to be 9043.45 erg/Oe, where H_c is the coercivity field, M_s is the saturation magnetization and M_r is the remanent magnetization.

3.6. Temperature dependent susceptibility

The temperature dependent susceptibility, (i.e., both ZFC and FC susceptibility of $Mn_{0.5}Zn_{0.5}Cr_2O_4$ nanoparticles at 100 Oe) are presented in Fig. 8. Both the ZFC and FC curves linearly increase up to 19 K, which was attributed to the normal transition temperature. The value of normal transition temperature (T_N) is greater than that

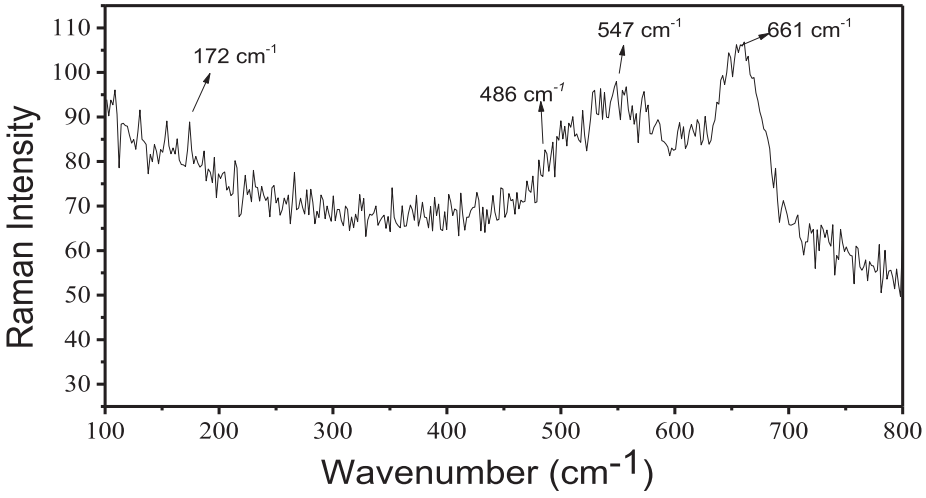

Fig. 6. Raman spectrum of $Mn_{0.5}Zn_{0.5}Cr_2O_4$ nanoparticles.

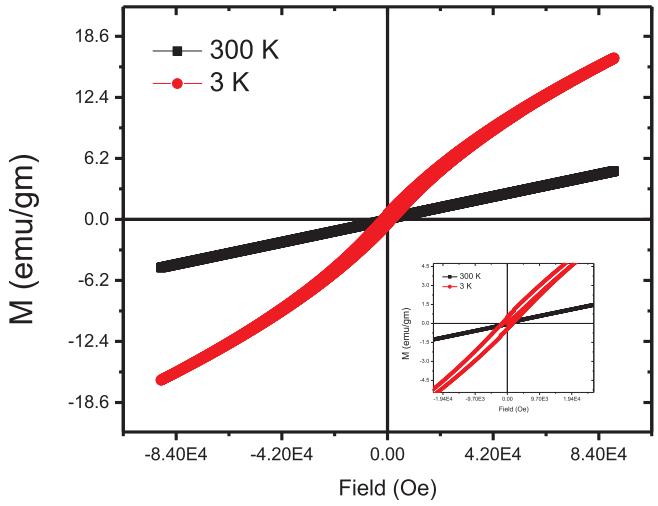

Fig. 7. Magnetic field dependent magnetization at 300 K, 3 K for $Mn_{0.5}Zn_{0.5}Cr_2O_4$ nanoparticles.

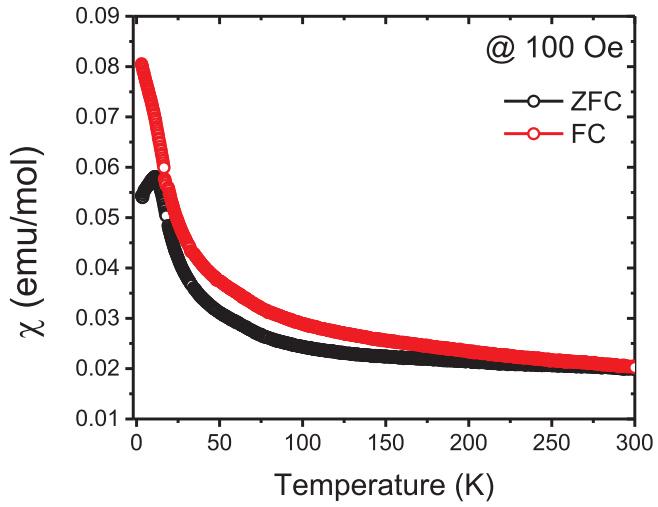

Fig. 8. Temperature dependent susceptibility under zero field cooling (ZFC) and field cooling (FC) at 100 Oe for $Mn_{0.5}Zn_{0.5}Cr_2O_4$ nanoparticles.

reported for a $ZnCr_2O_4$ bulk polycrystalline sample [39]. Fig. 8 shows a transition from paramagnetic to antiferromagnetic phase. With further temperature cooling, the susceptibility returns to increase the FC curve and decrease the ZFC path up to 2 K, which may be attributed to contributions from uncompensated surface spins of $Mn_{0.5}Zn_{0.5}Cr_2O_4$ nanoparticles.

We cannot observe a ferromagnetic nature in $Mn_{0.5}Zn_{0.5}Cr_2O_4$ nanoparticles due to non-magnetic Zn^{2+} ions at the tetrahedral site. Zinc contains chromate spinels which act as a good model of geometrically-frustrated magnets and it highly spins frustrated magnets even in the form of small dimensioned nanoparticles. These facts were confirmed by the high value of Curie-Weiss temperature (θ_{cw}) relative to the normal transition temperature (T_N). The paramagnetic and antiferromagnetic nature can be clearly observed in our sample.

For antiferromagnetic chromites with a non-magnetic octahedral site (A-site) atom, the effective magnetic moment (μ_{eff}) and the Curie-Weiss temperature (θ_{cw}) can be determined by fitting the observed magnetization to the Curie-Weiss law equation: $\chi = \chi_p + \frac{c}{T-\theta_{cw}}$, where χ_p is the temperature independent paramagnetic term which appears in susceptibility [5]. The value of the effective magnetic moment and the Curie-Weiss temperature are obtained by fitting the inverse of susceptibility (χ^{-1}) versus temperature data above the normal transition temperature (Fig. 9). The Curie-Weiss temperature (θ_{cw}) and effective magnetic moment (μ_{eff}) were found to be −428.87 K and 10.88 μ_B/f. u.,

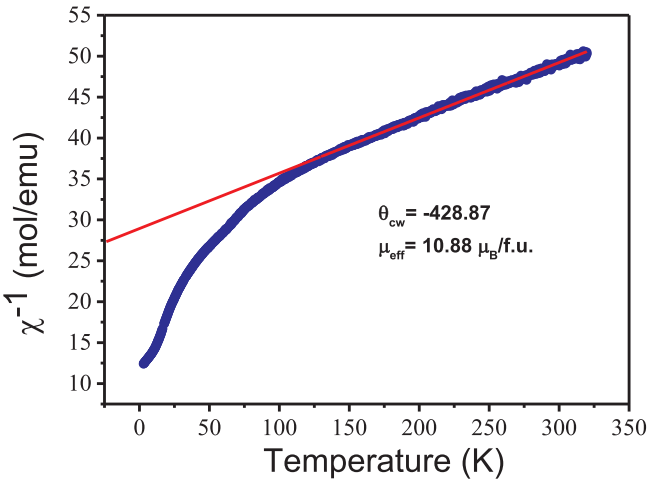

Fig. 9. Temperature dependent inverse susceptibility for $Mn_{0.5}Zn_{0.5}Cr_2O_4$ nanoparticles.

respectively. The obtained effective magnetic moment value matches well with the theoretical effective magnetic moment (Theoretical μ_{eff} = 9.786 μ_B/f). The frustration factor of $Mn_{0.5}Zn_{0.5}Cr_2O_4$ nanoparticles is found to be $|\theta_{cw}|/T_N$ = 22.57, and this value is greater than that for $ZnCr_2O_4$ nanoparticles $|\theta_{cw}|/T_N$ = 18 [5,40].

3.7. DFT calculations

In this section we conduct a theoretical evaluation about the effect of Zn substituted on the structural, magnetic and electronic properties of the $MnCr_2O_4$ material. First, the optimized lattice parameters for pure $MnCr_2O_4$ at the B3LYP theory level (a = b = c = 8.473 Å) showed reasonable agreement with the experimental results reported in Section 3.1. In this case, tetrahedral [MnO_4] clusters containing four equal Mn−O bonds of 2.049 Å oxygen-bridged with octahedral regular [CrO_6] clusters with six Cr−O bonds of 2.002 Å describe the crystalline structure of pure $MnCr_2O_4$. A contraction of the unit cell was observed (a = b = c = 8.417 Å) for the Zn substituted model, being in agreement with the Mn^{2+} and Zn^{2+} ionic radii experimental evidence. Thus, the Mn-O, Zn-O and Cr−O bond interactions were evaluated in order to establish the connection between the local disorders generated from the Zn substitution in the $MnCr_2O_4$ matrix. The unit cell contraction is accompanied by a shrinkage of A−O bond paths which becomes 2.003 Å and 2.040 Å for Zn−O and Mn−O, respectively. In addition, structural disorder provoked by the Zn substitution was observed in the [CrO_6] clusters which becomes distorted with four short Cr-O bonds of 1.987 Å and two long Cr-O bond paths of 2.006 Å. This fact can be attributed to the different ionic radii of divalent Zn and Mn cations, generating new distribution of the electron density for the substituted material.

Let us now briefly analyze the role of Zn substitution on the exchange coupling constant of $MnCr_2O_4$ material. First, the exchange coupling constant for pure $MnCr_2O_4$ was calculated using the Ising model as $J_{Mn\text{-}Mn}$ = −18.81 K, $J_{Cr\text{-}Mn}$ = −13.83 K and $J_{Cr\text{-}Cr}$ = −30.08 K, showing excellent agreement with previous theoretical and experimental results [41–44]. In this case, all exchange coupling constants were calculated to be antiferromagnetic, with $J_{Cr\text{-}Cr}$ being dominant along the investigated interactions. Thus, a ferromagnetic super-exchange mediated by oxygen p orbital is expected for this exchange coupling constant, following the guidelines by Goodenough-Kanamori-Anderson [45] in a regular 90°Cr-O-Cr cluster. However, the observed antiferromagnetic exchange coupling indicates the dominant character involving d orbital overlapping that result in an antiparallel interaction. On the other hand, the calculated $J_{Cr\text{-}Cr}$ and $J_{Mn\text{-}Cr}$ interactions for the Zn substitution model were −14.80 K and −30.63 K, respectively, indicating an overall intensification of the antiferromagnetic character mainly for the dominating Cr-Cr interactions. This fact can be addressed for the local structural disorder generated from the Zn substitution which shrinks the A−O bond interactions followed by a Jahn-Teller distortion along the [CrO_6] clusters. In addition, the calculated results indicate that a non-collinear magnetic ground state is the most suitable representation of the long-range antiferromagnetic interactions in pure and Zn substituted $MnCr_2O_4$ materials due to the competing behavior of the calculated exchange coupling constant [41–44].

Another point is that the experimental evidence of paramagnetic behavior at room temperature can be associated with the spin disorder along the exposed surfaces of pure and substituted $MnCr_2O_4$ nanoparticles, as reported for other materials [46–48]. In this case, the role of uncompensated spins along the exposed planes were not considered in this work, being a subject for further future studies.

Next, the electronic structure of pure and Zn substituted $MnCr_2O_4$ was investigated by means of the Band Structure and Density of States profiles, as presented in Fig. 10, considering the Neel ferromagnetic configuration (FIM-1) which corresponds to the most stable model in comparison to FEM. In this case, it was observed that the Valence Band

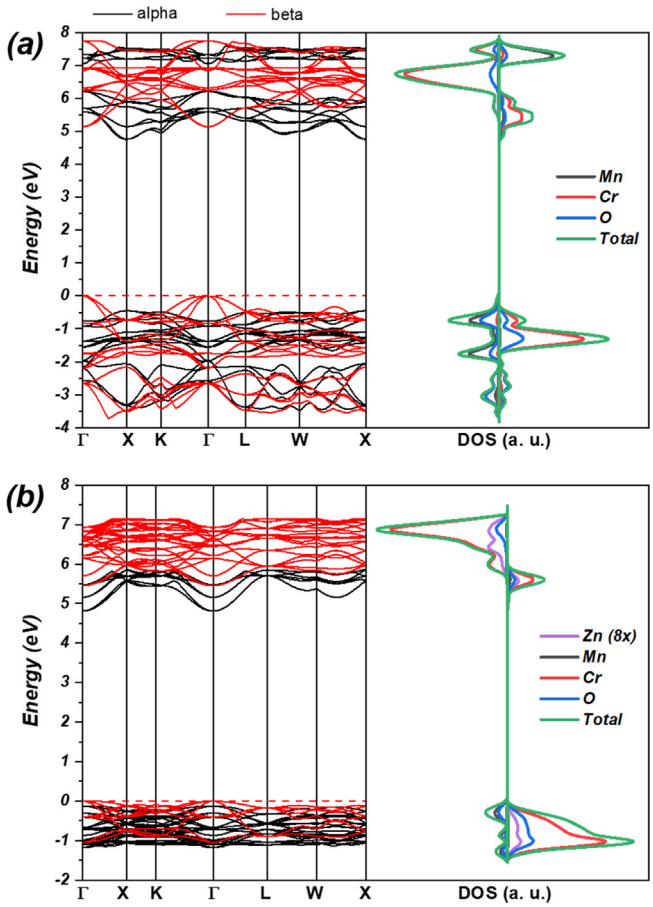

Fig. 10. Band Structure and atom-resolved Density of States profiles for (a) $MnCr_2O_4$ and (b) $Mn_{0.5}Zn_{0.5}Cr_2O_4$.

(VB) for pure $MnCr_2O_4$ (Fig. 10a) is composed of Cr and Mn (3d) orbitals hybridized with O (2p) states, while the Conduction Band (CB) is mainly composed of empty states of both Mn and Cr orbitals. Regarding the band-gap region, a direct electronic transition between Γ- Γ points was calculated around 5.14 eV for the spin-beta channel, while the spin-up shows higher energy excitation (5.21 eV between X and X), confirming the semiconductor behavior of $MnCr_2O_4$. On the other hand, it was observed that the VB for the Zn substituted material (Fig. 10b) is mainly composed of Cr (3d) orbitals hybridized with O (2p) states, with a minor contribution of Mn and Zn states, as well as for the CB. In addition, the substitution of Mn by Zn induces a disturbance on the VB maximum and CB minimum, narrowing the band-gap to 4.93 eV for the spin-up channel between Γ-Γ points, whereas the band-gap for the beta-spin channel was calculated as 5.47 eV. Such band-gap disturbance can be addressed to the new distribution of the electron density associated with the structural disorders generated from the substitution mechanism, especially for [CrO_6] clusters acting on the crystal field splitting of 3d energy levels for Cr, resulting in reduced excitation energy.

4. Conclusions

In this work, nanocrystalline $Mn_{0.5}Zn_{0.5}Cr_2O_4$ nanoparticles were successfully synthesized via the solution combustion method for the first time and deeply investigated by combining theoretical and experimental techniques. The XRD pattern reveals pure phase of the synthesized sample with the average crystallite size estimated to be 8 nm. Raman spectra assign the vibration modes of the sample, which agrees with the spinel cubic structure and the cations occupying the respective sites in the sample. In addition, theoretical calculations

suggest that the main role of Zn substituting on the structural properties of $MnCr_2O_4$ through a local structural distortion on the A—O (A = Mn, Zn) and Cr—O chemical bonds shrink the unit cell volume. The room temperature neutron diffraction study explored the origin for magnetic structure in the sample. Field dependent magnetic measurements at room temperature reveal the paramagnetic nature of the sample and low temperature, i.e. measurements at 3 K reveal the existence of hysteresis behavior, and the sample has antiferromagnetic behavior. The possible magnetic parameters were estimated from the M-H loop and DFT calculations for the first-neighbor exchange coupling constant. The susceptibility of ZFC and FC curves of the sample reveals the normal transition temperature is greater than that of the reported values of the $ZnCr_2O_4$ in bulk regime. The frustration factor was found to be greater than for $ZnCr_2O_4$ nanoparticles. Paramagnetic to antiferromagnetic phase transition was established in the present investigation of $Mn_{0.5}Zn_{0.5}Cr_2O_4$ nanoparticles, while the computed exchange coupling constant indicates the dominant antiferromagnetic character of Cr-Cr interaction. Additional electronic structure analysis indicated a narrowed band-gap for $Mn_{0.5}Zn_{0.5}Cr_2O_4$, enabling the reported nanoparticles as excellent candidates to achieve lower transition temperatures and superior electronic/optical properties.

Declaration of Competing Interest

The authors declare that they have no known competing financial interests or personal relationships that could have appeared to influence the work reported in this paper.

Acknowledgments

K. Manjunatha would like to express sincere thanks to the University Management for providing a fellowship for pursuing the Ph.D. program. This work was supported by the Federal University of São Carlos, the Federal University of Rio Grande do Norte (*PPGCEM-UFRN*), the State University of Ponta Grossa, CAPES, CNPq, and the Fundação Araucária (Brazil). R. A. P. Ribeiro acknowledges financial support from CNPq 156176/2018-1. M. C. Oliveira acknowledges financial support from *PNPD*/CAPES (2019/88887.319041). E. Longo acknowledges financial support from FAPESP 2013/07296-2. Dr. Jagadeesha Angadi V would like to express sincere thanks to UGC-DAE CSR, Mumbai Centre, BARC Campus, Trombay, Mumbai 400085, India for providing Neutron diffraction and Magnetic measurement facility.

Appendix A. Supplementary data

Supplementary data to this article can be found online at https://doi.org/10.1016/j.jmmm.2020.166595.

References

[1] M. Kamran, K. Nadeem, M. Mumtaz, Negative and anomalous T-dependent magnetization trend in $CoCr_2O_4$ nanoparticles, Solid State Sci. 72 (2017) 21–27.
[2] S. Chamyani, A. Salehirad, N. Oroujzadeh, D.S. Fateh, Effect of fuel type on structural and physicochemical properties of solution combustion synthesized $CoCr_2O_4$ ceramic pigment nanoparticles, Ceram. Int. 44 (2018) 7754–7760.
[3] V. Jagadeesha Angadi, A.V. Anupama, R. Kumar, S. Matteppanavar, B. Rudraswamy, B. Sahoo, Observation of enhanced magnetic pinning in Sm^{3+} substituted nanocrystalline MnZn ferrites prepared by propellant chemistry route, J. Alloy. Compd. 682 (2016) 263–274.
[4] K.M. Srinivasamurthy, J.V. Angadi, S.P. Kubrin, S. Matteppanavar, D.A. Sarychev, P.M. Kumar, H.W. Azale, B. Rudraswamy, Tuning of ferrimagnetic nature and hyperfine interaction of Ni^{2+} doped cobalt ferrite nanoparticles for power transformer applications, Ceram. Int. 44 (2018) 9194–9203.
[5] M.A. Kassem, A. Abu El-Fadl, A.M. Nashaat, H. Nakamura, Structure optical and varying magnetic properties of insulating MCr_2O_4 (M= Co, Zn, Mg and Cd) nanospinels, J. Alloy. Compd. 790 (2019) 853–862.
[6] A.L. Wysocki, T. Birol, Magnetically induced phonon splitting in ACr_2O_4 spinels from first principles, Phys. Rev. B 93 (2016) 134425.
[7] V. Kocsis, S. Bordács, D. Varjas, K. Penc, A. Abouelsayed, C.A. Kuntscher, K. Ohgushi, Y. Tokura, I. Kézsmárki, Magnetoelasticity in ACr_2O_4 spinel oxides (A =Mn, Fe Co, Ni, and Cu), Phys. Rev. B 87 (2013) 064416.
[8] M. Younis, M. Saleem, S. Atiq, S. Naseem, Magnetic phase transition and magneto-dielectric analysis of spinel chromites: MCr_2O_4 M = Fe, Co and Ni, Ceram. Int. 44 (2018) 10229–10235.
[9] D. Zákutná, A. Alemayehu, J. Vlček, K. Nemkovski, C.P. Grams, D. Nižňanský, D. Honecker, S. Disch, Critical size limits for collinear and spin-spiral magnetism in $CoCr_2O_4$, Phys. Rev. B 100 (2019) 184427.
[10] G.T. Lin, Y.Q. Wang, X. Luo, J. Ma, H.L. Zhuang, D. Qian, L.H. Yin, F.C. Chen, J. Yan, R.R. Zhang, S.L. Zhang, W. Tong, W.H. Song, P. Tong, X.B. Zhu, Y.P. Sun, Magnetoelectric and Raman spectroscopic studies of monocrystalline $MnCr_2O_4$, Phys. Rev. B 97 (2018) 064405.
[11] Z. Mousavi, F. Soofivand, M. Esmaeili-Zare, M. Salavati-Niasari, S. Bagheri, $ZnCr_2O_4$ nanoparticles: facile synthesis characterization and photocatalytic properties, Sci. Rep. 6 (2016) 20071.
[12] S. Rahman, H. Saqib, J. Zhang, D. Errandonea, C. Menéndez, C. Cazorla, S. Samanta, X. Li, J. Lu, L. Wang, Pressure-induced structural and semiconductor-semiconductor transitions in $Co_{0.5}Mg_{0.5}Cr_2O_4$, Phys. Rev. B 97 (2018) 174102.
[13] E.A.C. Miranda, J.F.M. Carvajal, A.A.L. Sepúlveda, J.C.R. Gutierrez, O.J.R. Baena, Properties of ceramic pigment $Zn_{0.5}Cu_{0.5}Cr_2O_4$ synthesized by solution combustion method, in: S.J. Ikhmayies, B. Li, J.S. Carpenter, J.-.Y. Hwang, S.N. Monteiro, J. Li, D. Firrao, M. Zhang, Z. Peng, J.P. Escobedo-Diaz, C. Bai (Eds.), Characterization of Minerals, Metals, and Materials 2016, Springer International Publishing, Cham, 2016, pp. 721–727.
[14] K. Le Dang, M.C. Mery, P. Veillet, Spin-glass-like behaviour of the mixed spinel systems $Mn_xZn_{1-x}Cr_2O_4$ and $Mn_{0.75}Mg_{0.25}(Cr_{1-y}V_y)_2O_4$, J. Magn. Magn. Mater. 43 (1984) 161–165.
[15] F. Leccabue, B.E. Watts, D. Fiorani, A.M. Testa, J. Alvarez, V. Sagredo, G. Bocelli, Crystal growth and magnetic characterization of $Zn_{1-x}Mn_xCr_2O_4$ single crystals, J. Mater. Sci. 28 (1993) 3945–3950.
[16] G.T. Lin, X. Luo, Q.L. Pei, F.C. Chen, C. Yang, J.Y. Song, L.H. Yin, W.H. Song, Y.P. Sun, Magnetic evolution of spinel $Mn_{1-x}Zn_xCr_2O_4$ single crystals, RSC Adv. 6 (2016) 56839–56844.
[17] K.C. Patil, S.T. Aruna, T. Mimani, Combustion synthesis: an update, Curr. Opin. Solid State Mater. Sci. 6 (2002) 507–512.
[18] K.M. Srinivasamurthy, K. Manjunatha, E.I. Sitalo, S.P. Kubrin, I.C. Sathish, S. Matteppanavar, B. Rudraswamy, V. Jagadeesha Angadi, Effect of Ce_{3+} substitution on the structural, morphological, dielectric, and impedance spectroscopic studies of Co–Ni ferrites for automotive applications, Indian J. Phys. (2019).
[19] R. Dovesi, A. Erba, R. Orlando, C.M. Zicovich-Wilson, B. Civalleri, L. Maschio, M. Rérat, S. Casassa, J. Baima, S. Salustro, B. Kirtman, Quantum-mechanical condensed matter simulations with CRYSTAL, Wiley Interdiscipl. Rev. Comput. Mol. Sci. 8 (2018) e1360.
[20] A.D. Becke, Density-functional thermochemistry. III. The role of exact exchange, J. Comput. Chem. 98 (1993) 5648–5652.
[21] C. Lee, W. Yang, R.G. Parr, Development of the Colle-Salvetti correlation-energy formula into a functional of the electron density, Phys. Rev. B 37 (1988) 785–789.
[22] H.J. Monkhorst, J.D. Pack, Special points for Brillouin-zone integrations, Phys. Rev. B 13 (1976) 5188–5192.
[23] M. Catti, G. Sandrone, G. Valerio, R. Dovesi, Electronic, magnetic and crystal structure of Cr_2O_3 by theoretical methods, J. Phys. Chem. Solids 57 (1996) 1735–1741.
[24] M.D. Towler, N.L. Allan, N.M. Harrison, V.R. Saunders, W.C. Mackrodt, E. Aprà, Ab initio study of MnO and NiO, Phys. Rev. B 50 (1994) 5041–5054.
[25] J.E. Jaffe, A.C. Hess, Hartree-fock study of phase changes in ZnO at high pressure, Phys. Rev. B 48 (1993) 7903–7909.
[26] R.A.P. Ribeiro, S.R. de Lazaro, C. Gatti, The role of exchange–correlation functional on the description of multiferroic properties using density functional theory: the $ATiO_3$ (A = Mn, Fe, Ni) case study, RSC Adv. 6 (2016) 101216–101225.
[27] R.A.P. Ribeiro, S.R. de Lazaro, S.A. Pianaro, Density Functional Theory applied to magnetic materials: Mn_3O_4 at different hybrid functionals, J. Magn. Magn. Mater. 391 (2015) 166–171.
[28] S. Rayaprol, R.A.P. Ribeiro, K. Singh, V.R. Reddy, S.D. Kaushik, S.R. de Lazaro, Experimental and theoretical interpretation of magnetic ground state of $FeMnO_3$, J. Alloy. Compd. 774 (2019) 290–298.
[29] J.K. Galivarapu, D. Kumar, A. Banerjee, C. Rath, Magnetic transitions in chemically synthesized nanoparticles of $CoCr_2O_4$, IEEE Trans. Magn. 52 (2016) 1–6.
[30] Q. Zhou, J. Wang, R. Zheng, Y. Gong, J. Lin, One-step mild synthesis of Mn-based spinel $Mn^{II}Cr_2^{III}O_4/Mn^{II}Mn_2^{III}O_4$/C and Co-based spinel $CoCr_2O_4$/C nanoparticles as battery-type electrodes for high-performance supercapacitor application, Electrochim. Acta 283 (2018) 197–211.
[31] V. Jagadeesha Angadi, B. Rudraswamy, K. Sadhana, K. Praveena, Effect of Sm^{3+}-Gd^{3+} co-doping on dielectric properties of Mn-Zn ferrites synthesized via combustion route, Mater. Today Proc. 3 (2016) 2178–2186.
[32] R. Kumar, R. Padam, D. Das, S. Rayaprol, V. Siruguri, D. Pal, Low temperature neutron diffraction studies on $Co(Cr_{1-x}Fe_x)_2O_4$ x = 0.05 and 0.075, RSC Adv. 6 (2016) 93511–93518.
[33] K. Manjunatha, I.C. Sathish, S.P. Kubrin, A.T. Kozakov, T.A. Lastovina, A.V. Nikolskii, K.M. Srinivasamurthy, M. Pasha, V.J. Angadi, X-ray photoelectron spectroscopy and low temperature Mössbauer study of Ce^{3+} substituted $MnFe_2O_4$, J. Mater. Sci. Mater. Electron. 30 (2019) 10162–10171.
[34] J. Słoczyński, J. Janas, T. Machej, J. Rynkowski, J. Stoch, Catalytic activity of chromium spinels in SCR of NO with NH_3, Appl. Catal. B 24 (2000) 45–60.
[35] Y. Wang, A.-P. Jia, M.-F. Luo, J.-Q. Lu, Highly active spinel type $CoCr_2O_4$ catalysts for dichloromethane oxidation, Appl. Catal. B 165 (2015) 477–486.
[36] Z. Wang, P. Lazor, S.K. Saxena, G. Artioli, High-pressure raman spectroscopic study of spinel ZnCr2O4, J. Solid State Chem. 165 (2002) 165–170.

[37] Y. Gao, H. Chang, Q. Wu, H.-Y. Wang, Y.-B. Pang, F. Liu, H.-J. Zhu, Y.-H. Yun, Optical properties and magnetic properties of antisite-disordered $Ni_{1-x}Co_xCr_2O_4$ spinels, Trans. Nonferrous Metals Soc. China 27 (2017) 863–867.
[38] T. Ramachandran, F. Hamed, The effect of fuel to nitrates ratio on the properties of $FeCr_2O_4$ nanopowders, Mater. Res. Bull. 95 (2017) 104–114.
[39] X.H. Chen, H.T. Zhang, C.H. Wang, X.G. Luo, P.H. Li, Effect of particle size on magnetic properties of zinc chromite synthesized by sol–gel method, Appl. Phys. Lett. 81 (2002) 4419–4421.
[40] H. Ueda, H. Mitamura, T. Goto, Y. Ueda, Field-Induced Metamagnetic Transitions in S = 3/2 Heisenberg Antiferromagnets MCr_2O_4, Prog. Theor. Phys. Suppl. 159 (2005) 256–259.
[41] J.-R. Huang, C. Cheng, Cation and magnetic orders in $MnFe_2O_4$ from density functional calculations, J. Appl. Phys. 113 (2013) 033912.
[42] F.F. Fava, I. Baraille, A. Lichanot, C. Larrieu, R. Dovesi, On the structural, electronic and magnetic properties of spinel, J. Phys. Condens. Matter 9 (1997) 10715–10724.
[43] E. Winkler, S. Blanco Canosa, F. Rivadulla, M.A. López-Quintela, J. Rivas, A. Caneiro, M.T. Causa, M. Tovar, Magnetocrystalline interactions in $MnCr_2O_4$ spinel, Phys. Rev. B 80 (2009) 104418.
[44] C. Ederer, M. Komelj, Magnetic coupling in $CoCr_2O_4$ and $MnCr_2O_4$: an LSDA + U study, Phys. Rev. B 76 (2007) 064409.
[45] J.B. Goodenough, Magnetism and the Chemical Bond, Interscience Publishers, 1963.
[46] R.A.P. Ribeiro, L.H.S. Lacerda, E. Longo, J. Andrés, S.R. de Lazaro, Towards enhancing the magnetic properties by morphology control of $ATiO_3$(A = Mn, Fe, Ni) multiferroic materials, J. Magn. Magn. Mater. 475 (2019) 544–549.
[47] R.A.P. Ribeiro, S.R. de Lazaro, L. Gracia, E. Longo, J. Andrés, Theoretical approach for determining the relation between the morphology and surface magnetism of Co_3O_4, J. Magn. Magn. Mater. 453 (2018) 262–267.
[48] R.A.P. Ribeiro, J. Andrés, E. Longo, S.R. Lazaro, Magnetism and multiferroic properties at $MnTiO_3$ surfaces: a DFT study, Appl. Surf. Sci. 452 (2018) 463–472.